Thermal–hydrodynamic–chemical (THC) modeling based on geothermal field data

Alexey Kiryukhin[a,*], Tianfu Xu[b], Karsten Pruess[b], John Apps[b], Igor Slovtsov[a]

[a]*Institute of Volcanology Piip-9, Petropavlovsk-Karnchatsky, 683006, Russia*
[b]*Earth Sciences Division, Lawrence Berkeley National Laboratory, MS590-1116, One Cyclotron Rd, Berkeley, CA 94720, USA*

Abstract

Data on fluid chemistry and rock mineralogy are evaluated for a number of geothermal fields located in the volcanic arc of Japan and Kamchatka, Russia, Common chemical characteristics are identified and used to define scenarios for detailed numerical modeling of coupled thermal–hydrodynamic–chemical (THC) processes. The following scenarios of parental geothermal fluid upflow were studied: (1) single-phase conditions, 260 °C at the bottom ('Ogiri' type); (2) two-phase conditions, 300 °C at the bottom ('Hatchobaru' type); and (3) heat pipe conditions, 260 °C at the bottom ('Matsukawa' type). THC modeling for the single-phase upflow scenario shows wairakite, quartz, K-feld spar and chlorite formed as the principal secondary minerals in the production zone, and illite-smectite formed below 230 °C. THC modeling of the two-phase upflow shows that quartz, K-feldspar (microcline), wairakite and calcite precipitate in the model as principal secondary minerals in the production zone. THC modeling of heat pipe conditions shows no significant secondary deposition of minerals (quartz, K-feldspar, zeolites) in the production zone. The influence of thermodynamic and kinetic parameters of chemical interaction, and of mass fluxes on mineral phase changes, was found to be significant, depending on the upflow regime. It was found that no parental geothermal fluid inflow is needed for zeolite precipitation, which occurs above 140 °C in saturated andesite, provided that the porosity is greater than 0.001. In

---

* Corresponding author. Tel.: +7-415-22-59344; fax: +7-415-22-54723.
E-mail address: avk2@kcs.iks.ru (A. Kiryukhin).

contrast, quartz and K-feldspar precipitation may result in a significant porosity reduction over a hundred-year time scale under mass flux conditions, and complete fracture sealing will occur given sufficient time under either single-phase or two-phase upflow scenarios. A heat pipe scenario shows no significant porosity reduction due to lack of secondary mineral phase deposition.

1. Introduction

The traditional analysis of geochemical evolution and rock alteration involves the separation of fluid flow and chemical species transport from chemical reactions, and the utilization of geochemical batch models such as CHILLER (Reed, 1982) and EQ3/6 (Wolery, 1992). However, the geochemical evolution in hydrothermal fractured rock systems occurs through a complex interplay of chemical reactions with multi-phase fluid and heat flow. Recently there has been growing interest in a comprehensive description of the coupled processes involved in reactive chemical transport in porous media (Steefel and Lasaga, 1994; White, 1995; Xu and Pruess, 2001a, b). The work presented in this paper employs the TOUGHREACT code (Xu and Pruess, 1998, 2001b) to model the interaction of ascending parental geothermal fluids with primary minerals. We employ a comprehensive description of the interplay between fluid flow, mass transport, and chemical reactions in systems with large temperature variations to examine whether our current understanding of these processes is sufficient to explain the secondary mineral assemblages observed in geothermal systems.

A number of geothermal fields associated with volcanic activity of the island arcs of the Kamchatka Peninsula and the Japanese islands are well characterized, and have thermal, hydrologic and geochemical features in common. They present an attractive target for testing coupled thermal–hydrodynamic–chemical (THC) simulation models. We first briefly summarize and discuss the thermodynamic and chemical characteristics of the Kamchatka and Japanese geothermal fields. This is followed by a presentation of our modeling approach, including a summary of the TOUGHREACT simulator. We then present and discuss results for a number of alternative scenarios, and evaluate the extent to which model predictions match field observations.

2. Geothermal field data

Fig. 1 shows the main geothermal fields of Kamchatka and Japan. Tables 1 and 2 present data on the fluid chemistry and mineralogy of these systems, which form the basis of the modeling studies presented in this paper. In the following paragraphs, we briefly summarize the principal features of the geothermal fields under study.
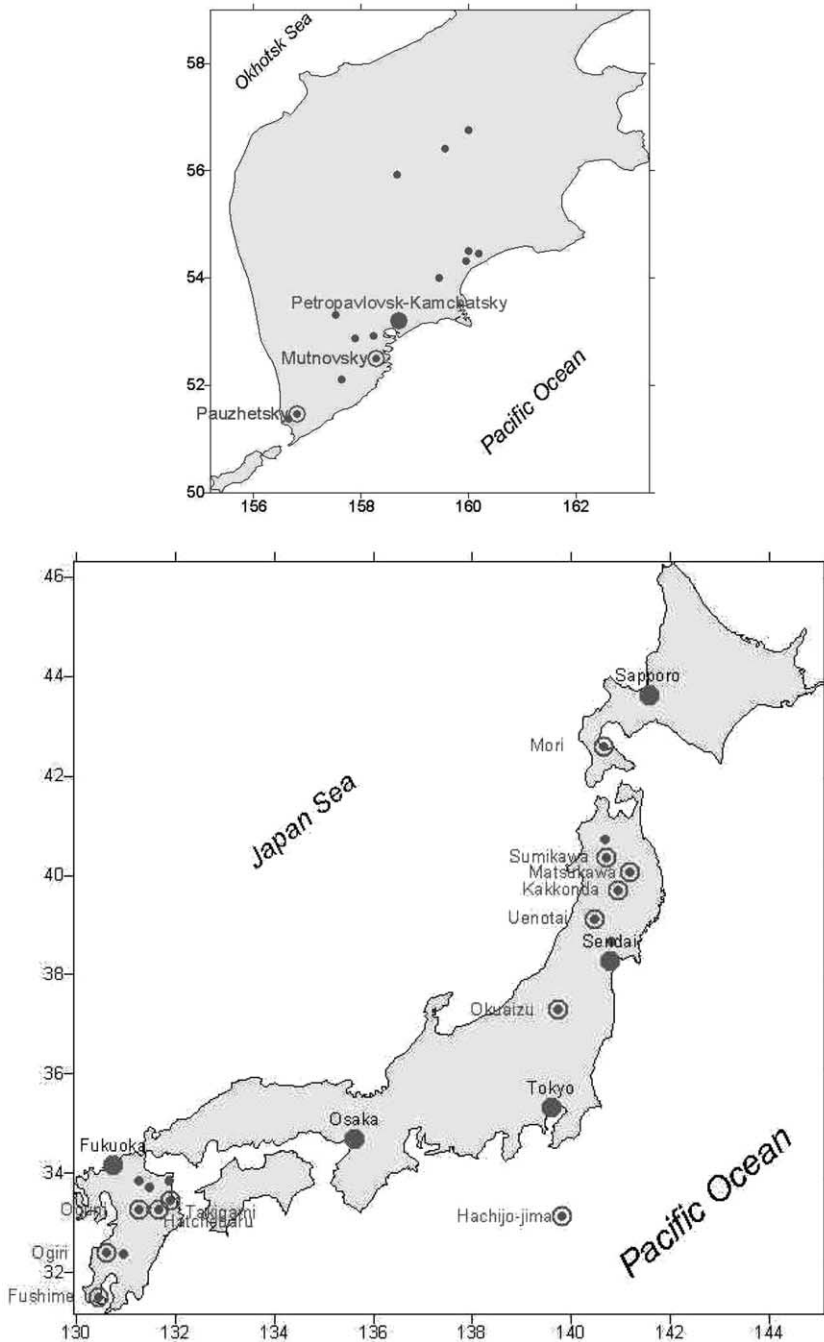
Fig. 1. Geothermal fields of Kamchatka (Russia) and Japan (small black dots). Large grey dots: main cities; circles with black dots: fields currently used for THC studies.

Table 1
Gas and fluid chemistry data of Japanese and Kamchatka (Russia) geothermal fields

Geothermal field, well	Enthalpy kJ/kg	pH 25	pH, cor.	Na	K	Ca	Mg	Fe	Al	Cl	SO_4	HCO_3	CO_3	As	B	SiO_2	CO_2	H_2S	H_2	R-gas
Nigorikawa,D-1	1150	8.2		5910	815	90.5	0.8	0.5	0.06	9540	393					486	8000			
Matsukawa,M-3	2800	5.6		0.35	0.11			0.2	0.02	1.6	0.16						12,580	1090		275
Sumikawa,SC1	1560	7.6	7.3	322	54.0	5.2	1.3	0.1	0.1	265	47.6	24.6		7.5	123.8	665	138	79	0.1	240
Kakkonda,19	1450	4.0	4.2	412	93.6	10.9	0.3	11.5	0.5	762	34.3			2.5	17.6	811	249	46	1	23
Uenotai,T-45	1692	9.5	7.3	94	19	0.2	0.0			122	1.1			0.1		412	1541	198	2.8	38
Okuaizu,87N-15T	1500		6.6	5202	1451	769	7.0	1.2	0.5	11,100	5					733	51,323	1429	0	159
Hachijo-jima,HT-1	2650	6.2	5.3	110	6.2	13.5	0.1			191	6.4	0.2					14,928	1190	19	22
Takigami,TT14	1025	9.1	8.0	385	68.2	6.4	0.1			602	73		41		7.5	455	446	46		16
Hatchobaru,H-17	1100	8.0	5.6	860	120	32	0.1			1430	96				23	510	8670	200		70
Oguni,GH20	1180	8.8	7.4	689	97.2	16	0.01	0.01	0.6	1175	42.1	41.3			15.1	446	269	5.6		8
Ogiri,NT-Al	963	8.7	7.7	335	40.6	8.4	0.01		0.9	453	150.4	12.2		0.0	29.5	477	31	1.8		
Fushime,19	1998	5.8	5.2	3628	1095	402	1.9			7872	22.7				27.2	319	2181	432	2	22
Mutnovsky,029W	1200	7.9	6.7	157	29.6	1.3	0.0			185	80.3	53.9				683	2140	435	2	
Pauzhetsky,106	820	8.5	7.4	595	47.3	39.6	0.0			1139	102	9.4		2.5	19.5	199	6			11

Concentrations are given in units of mg/kg and refer to deep reservoir conditions ('parental geothermal fluids'). The enthalpy data are used for steam and separated water species normalization. pH correction is based on the approach by Reed and Spycher (1984). R-gas—residual gases (N_2, Ar, CH_4, etc.).

Table 2
Principal secondary minerals in the production reservoirs of the geothermal fields

Geothermal field	Base temperature °C and phase conditions	Production reservoir host rocks	Principal secondary hydrothermal minerals occurrence													
			Quartz	K-feldspar	Na-feldspar	Wairakite	Laumontite	Calcite	Anhydrite	Chlorite	Illite	Smectites	Epidote	Prehnite	Sericite	Kaolinite
Mori (Nigorikawa)	270 liquid	Limestones, andesites						⊕								
Matsukawa	250 steam	Dacite and rhyolite welded tuffs													⊕	
Sumikawa	300 2-phase	Andesites and granites	⊕	⊕		⊕	⊕		⊕	⊕			⊕			
Kakkonda	340 liquid	Andesitic and dacitic tuffs	⊕	⊕					⊕				⊕	⊕	⊕	
Uenotai	300 2-phase liquid	Andesites and granite	⊕			⊕		⊕					⊕			
Okuaizu	300 liquid	Rhyolite and andesite tuffs		⊕				⊕	⊕	⊕						⊕
Hachijo-jima	300 liquid	Andesites and basalts	⊕			⊕		⊕	⊕							
Takigami	250 liquid	Andesitic and dacitic tuffs and lavas				⊕	⊕			⊕	⊕					
Hatchobaru	300 liquid	Pyroxene andesites	⊕		⊕		⊕	⊕	⊕	⊕			⊕			
Oguni	240 liquid	Dacitic tuffs and andesites						⊕								
Ogiri	232 liquid	Pyroxene andesites	⊕	⊕		⊕				⊕			⊕			
Fushime	300 liquid	Andesitic-dacitic lavas and tuffs		⊕	⊕					⊕			⊕			
Mutnovsky	300 liquid, 2-phase	Diorites, sandstones, rhyolite, andesite tuffs and lavas	⊕			⊕	⊕	⊕		⊕	⊕		⊕	⊕		
Pauzhetsky	220 liquid	Welded rhyolite tuffs, andesite tuffs and lavas	⊕	⊕			⊕	⊕		⊕						

2.1. Nigorikawa (Mori) (Higo, 1985)

The host reservoir rocks are limestones intruded by andesite dikes. An Na–Cl–CO_2 enriched (8 g/kg) liquid phase is present at 270 °C.

2.2. Matsukawa (Hanano and Matsuo, 1990)

The geothermal reservoir occupies dacite and rhyolite welded tuffs at the contact zone with a quartz diorite intrusion. Heat pipe conditions at pressures of 20–30 bar and temperatures of 200–240 °C are observed. Pyrophyllite is a principal secondary mineral in production zones.

2.3. Sumikawa (Ariki et al., 2000; Ueda et al., 1991)

The reservoir consists mainly of Tertiary altered andesite, intruded by granite. A production zone in two-phase conditions has temperatures of up to 300 °C and is traced by zeolites (wairakite), epidote and chlorite.

2.4. Kakkonda (Muraoka et al., 1998)

A neo-granitic pluton (0.19 Ma) found beneath this geothermal field acts as a magmatic heat source for the geothermal system. The reservoirs consist mainly of Miocene andesitic and dacitic tuffs. Production zones are in single-phase liquid conditions with temperatures of 220–260 °C (shallow reservoir) and 280–340 °C (deep reservoir). They are delineated by epidote, anhydrite, sericite, prehnite and K-feldspar. Abundant secondary minerals are quartz, chlorite, calcite and Ca-feldspar plagioclase. There were at least four heating events in the evolution of this field, which resulted in a very complicated superposition of secondary mineralization. An inflection point in the temperature profile of super-deep well WD-1a occurs at a depth of 3100 m and a temperature of 380 °C, and marks the expected brittle-plastic boundary and the maximum depth of hydrothermal convection. A two-phase zone of Na–Cl brine and non-condensible gas (CO_2, H_2S) exists as intra-crystalline fluid below the hydrothermal convection system.

2.5. Uenotai (Naka and Okada, 1992; Takeno, 2000)

The reservoir consists of Miocene andesite and pre-Tertiary granite. A central zone is in boiling conditions at a temperature of 300 °C, and is surrounded by a liquid-dominated zone. Production zones are traced by secondary quartz, epidote, calcite and zeolites (wairakite), while other zeolites (laumontite, mordenite) are found outside of the production zones.

2.6. Okuaizu (Mizugaki, 2000; Nitta et al., 1995)

The principal production zone occurs at a depth of 1.0–2.6 km within fractured Neogene "green tuff" formations (subaqueous volcanic rocks that have been altered

to a green color) along two northwest-trending faults to the southeast of the caldera: Chinokezawa and Sarukurazawa. High salinity Na–Cl (about 5–15 g/kg) and gas-enriched (CO_2, 10–80 g/kg) geothermal fluid circulation is characterized by the occurrence of calcite, anhydrite, chlorite and sericite at 250–300 °C. A shallow reservoir is delineated by K-feldspar. The upper part of the production zone is sealed mainly by smectite and mordenite.

2.7. Hachijo-jima *(Matsuyama et al., 2000)*

This high-temperature liquid-dominated system exists in fractures in Tertiary andesite and basalt formations. The fractures serve as conduits for the ascent of geothermal fluid, and act as a geothermal reservoir. Secondary minerals distributed in the upper part of the 300 °C upflow region are quartz, calcite and anhydrite. Production zones are characterized by wairakite.

2.8. Takigami *(Furuya et al., 2000)*

The reservoir host rocks are andesitic and dacitic tuffs and lava in two fault/fracture systems. The parent liquid phase is at 250 °C and discharges laterally. The production reservoir is traced by the distribution of illite-chlorite. The locations of the upper limit of the zeolite minerals, laumontite and wairakite, coincide with the current temperature contours, at about 150 and 200 °C, respectively.

2.9. Hatchobaru *(Fujino and Yamasaki, 1984; Hayashi et al., 1978)*

The reservoir host rocks include fractured pyroxene andesites interrupted by five main fault zones. The parent liquid is at 300 °C. Hydrothermal alteration associated with ascending fluid flow includes a silicified zone of zeolites and feldspar (with anhydrite and calcite), an aluminosilicate zone, and an alunite zone.

2.10. Oguni *(Yamada et al., 2000)*

The reservoir is composed of Quaternary dacitic pyroclastics and andesites. The parent liquid is at 240 °C. Calcium carbonate scaling was observed under wellbore flashing conditions. The secondary mineralogy has not been described, but is believed to be similar to that of the Pauzhetsky geothermal field (see below).

2.11. Ogiri *(Goko, 2000)*

This system is dominated by the Ginyu fault (70–75°E strike, 63–72°N dip, width of 20 m) and contains liquid at 232 °C in andesite host rocks. There is no indication of superposition or retrograde hydrothermal alteration. The distribution of hydro-thermal minerals is distinctly parallel to the isothermal contours. Wairakite and chlorite-smectite indicate the proximity to the Ginyu fault, and whether or not a well has been drilled completely through the fault zone. Secondary quartz, wairakite,

K-feldspar, chlorite and epidote are present in the production zone. The shallow impermeable zone, produced by self-sealing through the formation of smectite, has a 200–400 m vertical extent and overlies the Ginyu fault like an umbrella, acting as a cap rock.

2.12. Fushime (Okada et al., 2000)

The main reservoir is composed of andesitic-dacitic lavas and tuffs in two fracture zones developed around a dacite intrusion. One is a NNE–SSW trending zone to the west, and the other is a NW–SE trending zone to the south. In the main production zone temperatures exceed 300 °C at a depth of 1700 m below sea level. The Cl, Br/Cl ratios and stable isotope data indicate that the Fushime geothermal fluid originated from CO_2-enriched (up to 12.5 g/kg in steam phase) heated sea water ascending in single-phase conditions. The production zones are characterized by chlorite, epidote and K-feldspar, whereas Na-feldspar (albite) is found in the peripheral parts of the hydrothermal reservoir.

2.13. Mutnovsky (Dachny) (Kiryukhin, 1993, 1996)

Production occurs from a fault zone of approximately 80 m thickness with a north-east-north strike and 60° south-east-south dip. High-temperature liquid (40 kg/s, 1390 kJ/kg) upflows from southeast of the fracture, where a deep 280 °C liquid-dominated zone shows quartz-epidote-chlorite secondary hydrothermal mineralization. In the upper part of the main production zone, ascending fluids encounter two-phase conditions characterized by prehnite-wairakite precipitation. Fracture host rocks are diorites, Miocene-Pliocene sandstones, rhyolites and andesite tuffs and lavas. Shallow steam condensate and a meteoric water mixing zone are characterized by calcite-chlorite-illite mineralization.

2.14. Pauzhetsky (Pauzhetka, 1965)

Sub-lateral liquid flow at temperatures of 180–200 °C occurs at depths of 100–800 m within the highly permeabile Neogene-Quarternary psephytic tuffs. The dominant secondary minerals in the production zone are zeolites (mostly laumontite), feldspars, carbonates and chlorites. Feldspars form at 160–190 °C as albite and adularia, associated with laumontite and calcite. K-feldspar (adularia) occurs in the upper high-temperature zone, while Na-feldspar (albite) is present in lower-temperature (inversion) zones.

3. Model setup

The current conceptual understanding of THC processes in hydrothermal systems may be expressed as shown in Fig. 2. Cold meteoric water from a recharge area descends through sub-vertical channels, such as permeable faults, or sub-vertical
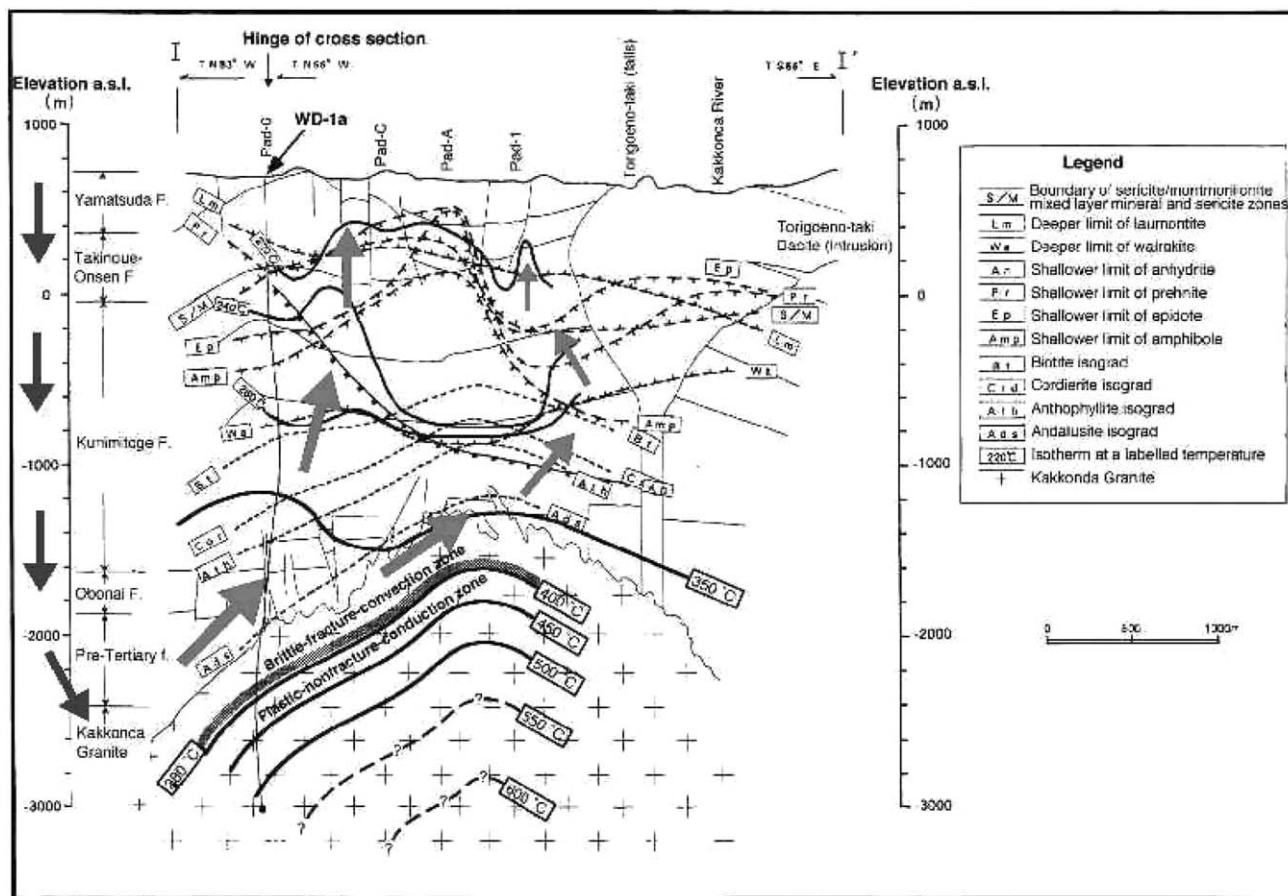
Fig. 2. Conceptual model of THC processes in a hydrothermal system, based on the example of Kakkonda geothermal field (Mutaoka et al., 1998). Suggested circulation patterns: downward arrows, meteoric recharge; upward arrows, ascending high-temperature geothermal fluids.

intrusive body contacts. At depth it is converted to high-temperature NaCl and CO_2 enriched 'parent geothermal fluid' through heat and chemical exchange. Basically, the 'parent geothermal fluid' of geothermal systems has two components: meteoric water and magmatic fluid. Deep-level magmatic fluid contributes gases such as HCl, HF, SO_2, H_2O, CO_2 and H_2S, which convert to dominant NaCl-CO_2 form due to interaction with host magmatic rocks. These fluids may in part become trapped below brittle/plastic boundaries of intrusions in the form of quartz polyphase NaCl–CO_2 inclusions (as proved by deep drilling in Kakkonda geothermal field; Muraoka et al., 1998). Then fluids ascend through high-permeability zones ('geothermal reservoirs'), and finally discharge at the earth surface in the form of hot springs and fumaroles. Flows from recharge to discharge areas are driven by pressure and fluid density differences (forced and free convection).

The principal secondary minerals involved in precipitation processes in reservoirs under high-temperature conditions include quartz, wairakite, K-feldspar, chlorite, epidote, calcite, anhydrite, prehnite and sericite (Table 2). Based on the above information, a simplified streamline numerical model of a hydrothermal system can be set up as a series of connected volume elements B1, R_n-elements and D1 (Fig. 3). B1 is a basement element, where the 'parental geothermal fluid' originates. The R_n-elements are sequentially connected reservoir elements; the 'parental geothermal fluid' ascends through these reservoir elements in set temperature and pressure steps. D1 is a discharge element, with assigned constant atmospheric pressure and surface temperature conditions (1 bar, 10 °C). Temperatures in all elements are kept constant by specifying artificially high rock densities (10^{15} kg/m³) in all elements of the model; steady-state fluid flow through the system was specified to simplify reactive chemical transport considerations. The following scenarios of parental geothermal fluid upflow in natural undisturbed conditions were studied: (1) single-phase upflow conditions, 260 °C at the bottom (e.g. Ogiri, Takigami, Oguni, and Pauzhetsky geothermal fields, and also Nigorikawa and Kakkonda shallow reservoirs); (2) two-phase upflow conditions at 300 °C (e.g. Hatchobaru, Sumikawa, Uenotai, Mutnovsky, Fushime, Okuaizu and Hachijo-jima); (3) heat pipe up-flow conditions, 260 °C at the bottom (e.g. Matsukawa). Temperature, pressure, saturation and steady flow conditions are specified according to the scenarios mentioned above and kept constant in all elements. These types of upflow conditions are illustrated by specific geological sections and pressure–temperature–saturation (P–T–S) logs of the geothermal fields (Figs. 4–6).

All simulations were performed with the TOUGHREACT code (Xu and Pruess, 1998, 2001a; see Appendix). The program was developed by introducing reactive chemistry into the framework of the existing multi-phase fluid and heat flow code TOUGH2 (Pruess, 1991). Tables A1 and A2 in the Appendix give the governing equations for fluid and heat flow, and chemical transport, that are solved by TOUGHREACT. The code employs a sequential iteration approach that solves the transport and reaction equations separately. Flow and transport are based on space discretization by means of integral finite differences (Narasimhan and Witherspoon, 1976). An implicit time-weighting scheme is used for individual components of the model, consisting of flow, transport, and kinetic geochemical reaction. The chemical
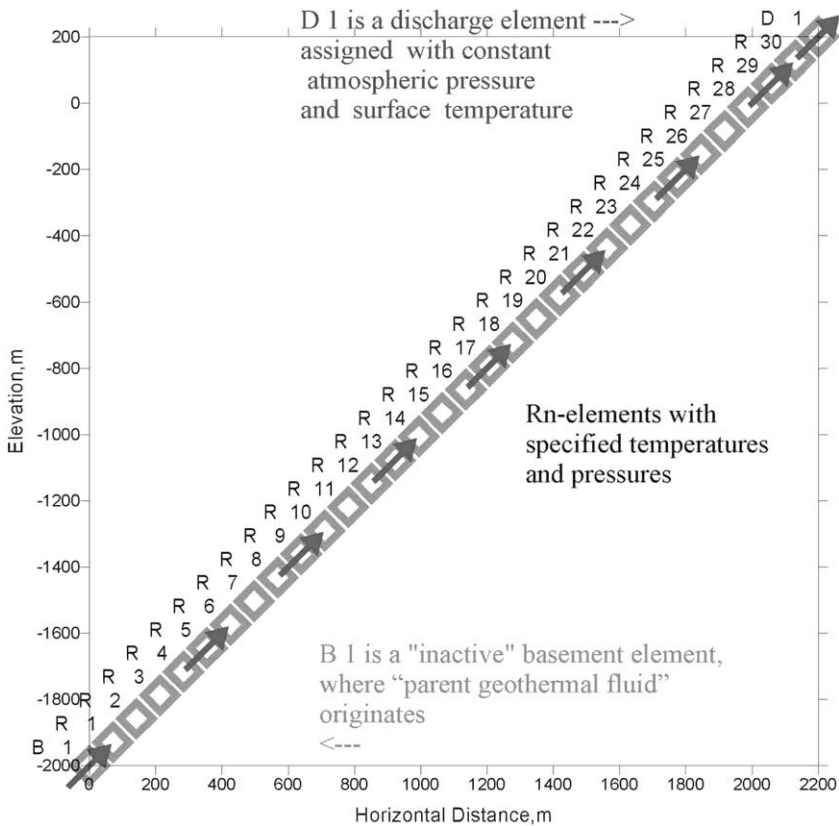
Fig. 3. Streamline model of ascending parent geothermal fluid flow in a geothermal reservoir, including the numerical grid, and initial and boundary conditions used in the model.

transport equations are solved independently for each component, whereas the reaction equations are solved on a grid-block basis using Newton–Raphson iteration. Full details of the code are given in Xu and Pruess (1998, 2001b). In the model, advective and diffusive transport of aqueous chemical species is considered. Aqueous chemical complexation is considered assuming local equilibrium. Mineral dissolution/precipitation can proceed at equilibrium and/or under kinetic conditions, according to the following rate law:

$$r = kS(1 - Q/K)\exp[E_a/(R^*298.15) - E_a/(RT)]$$

Here k is the chemical dissolution/precipitation kinetic rate constant at 25 °C, mol/s m^2; S is specific reactive surface area, m^2/m^3; Q is the activity product; K is the equilibrium constant for mineral–water interaction; E_a is the activation energy, kJ/kmol; R is the gas constant, kJ/kmol K, and T is temperature, K.

Temperature effects are also considered for geochemical reaction calculations in which equilibrium and kinetic data are functions of temperature. In the present
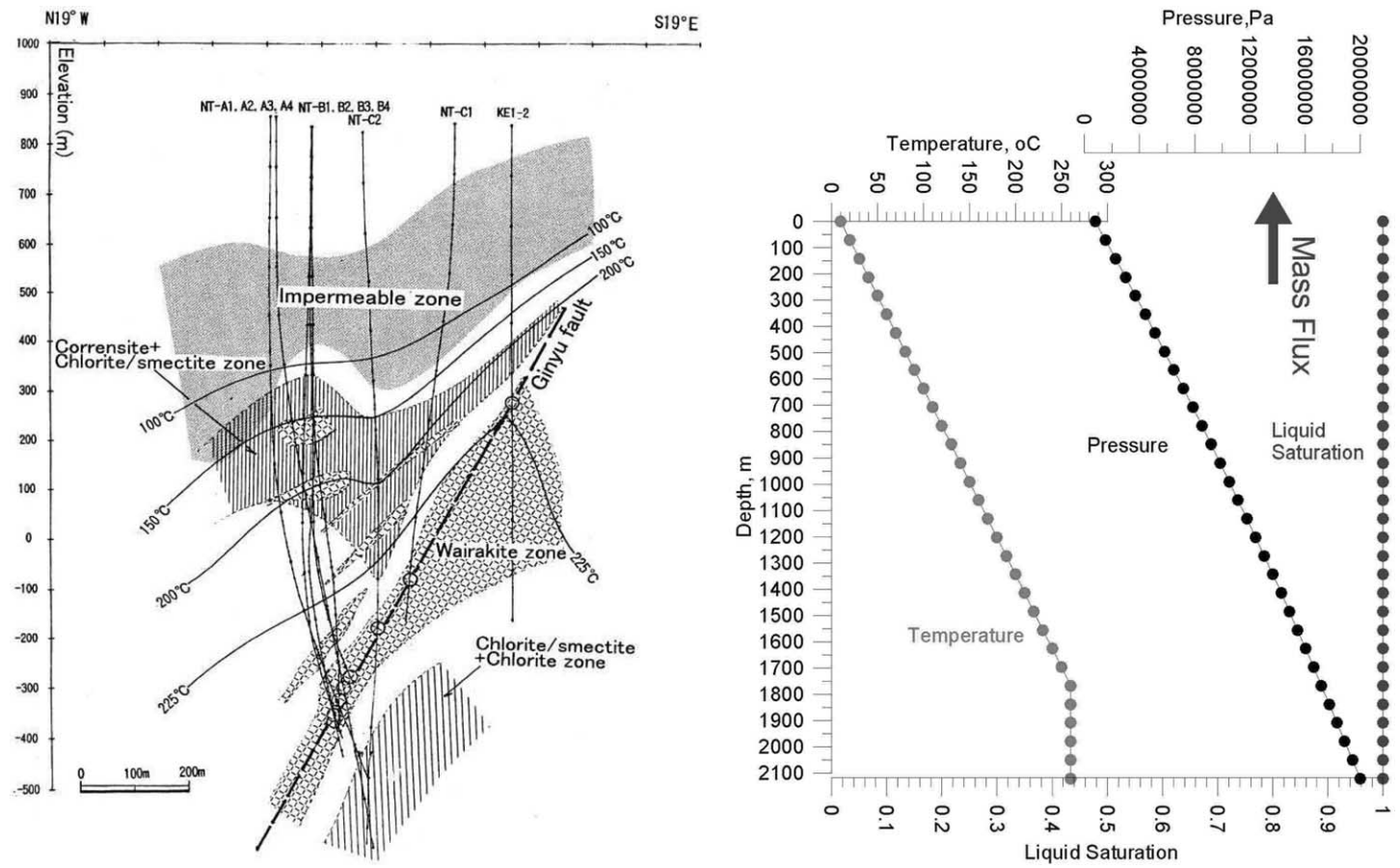
Fig. 4. Single-phase upflow scenario. Left side: cross-section showing the distribution of clay minerals and wairakite around the Ginyu fault zone, Ogiri field. All wells are projected onto the section perpendicular to the plane of the Ginyu fault. Open circles represent the Ginyu fault intersections in the production wells (Goko, 2000). Right side: model temperature, pressure and liquid saturation distribution corresponding to the scenario involving parental geothermal fluid upflow under single-phase conditions with a temperature of 260 °C at the bottom.
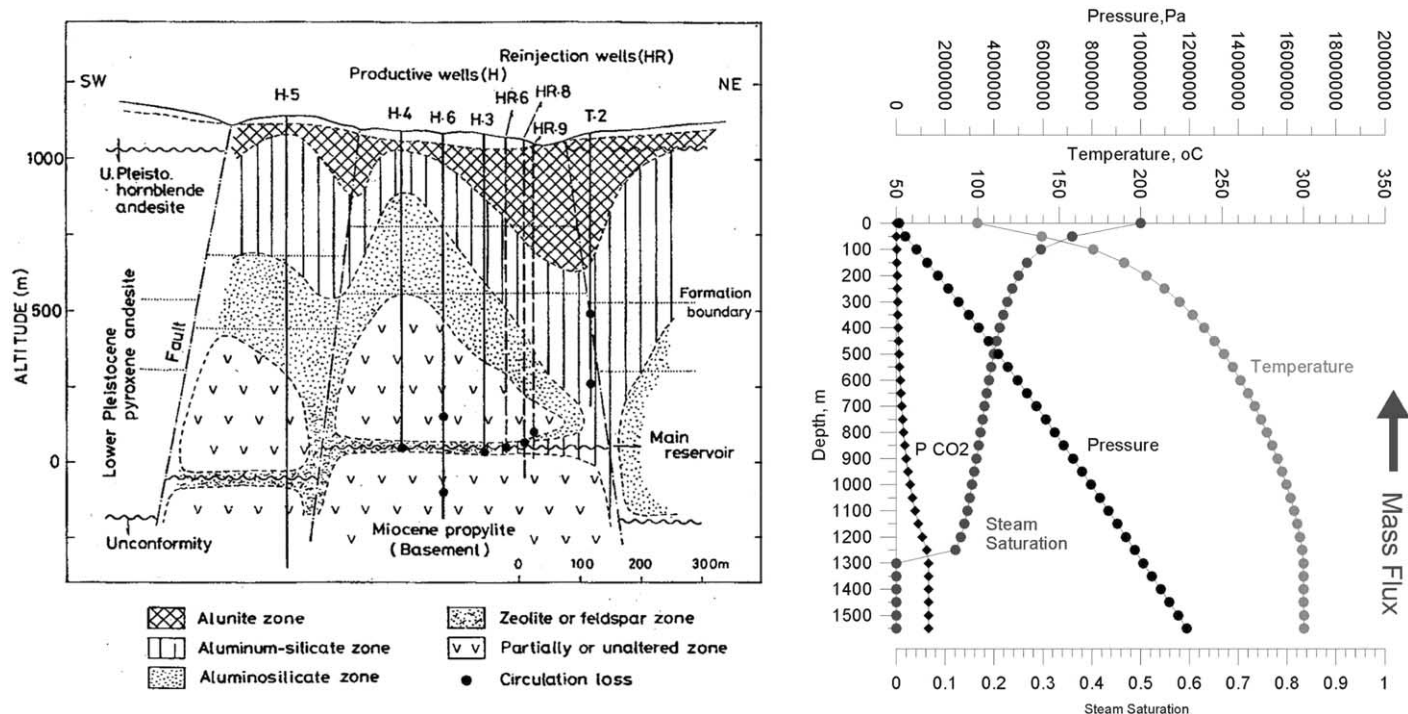
Fig. 5. Two-phase upflow scenario. Left side: schematic cross-section showing the geological setting and alteration around reinjection and production wells in the Hatchobaru geothermal field (Hayashi et al., 1978). Right side: model temperature, pressure and steam saturation distribution corresponding to the scenario involving parental geothermal fluid upflow under two-phase conditions at 300 °C at the bottom.
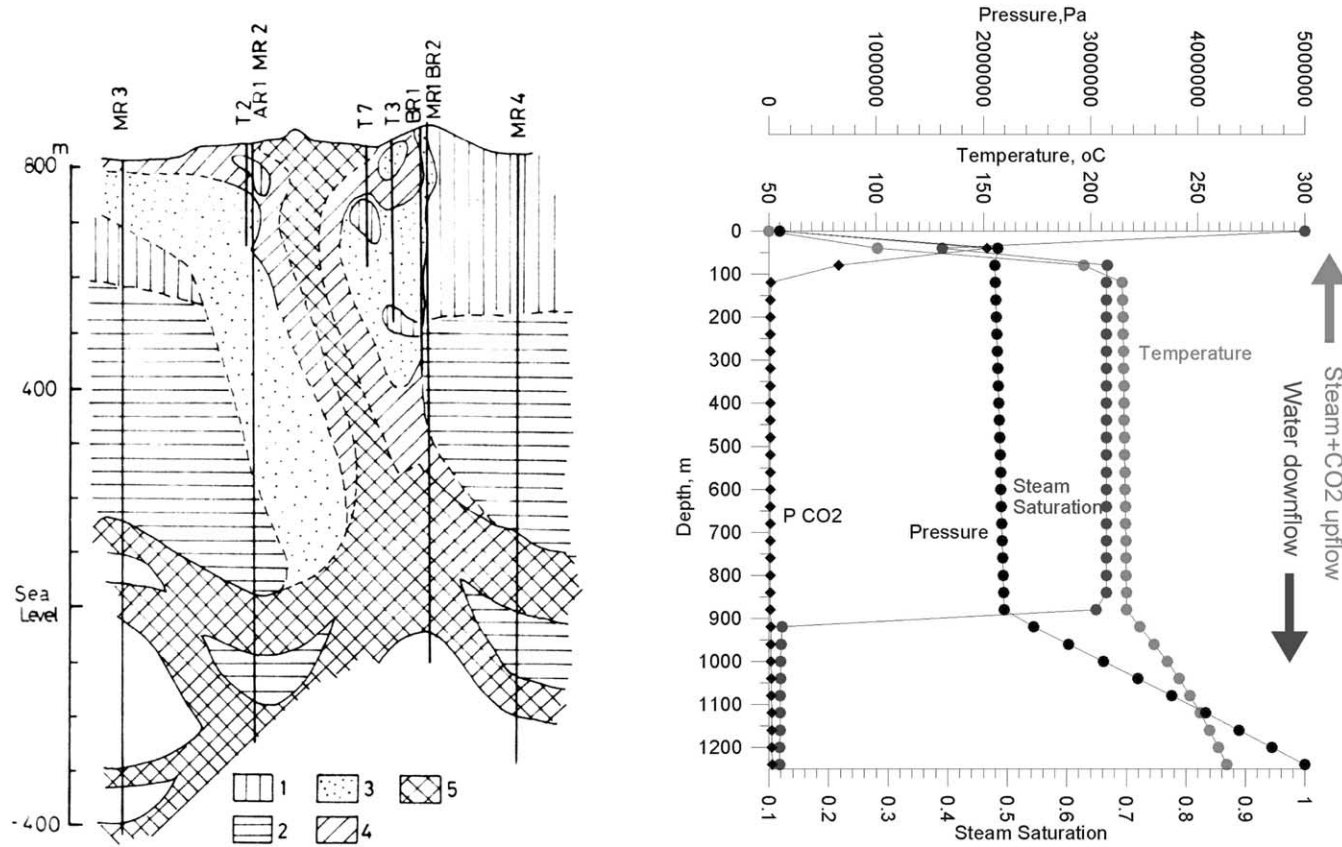
Fig. 6. Heat pipe upflow scenario. Left side: schematic cross-section of alteration zones in the Matsukawa geothermal field. 1—zone of montmorillonite and iron-rich saponite; 2—zone of chlorite; 3—zone of kaolinite; 4—zone of alunite; 5—zone of pyrophyllite (Yoshida, 1984). Right side: model temperature, pressure and steam saturation distribution corresponding to the scenario of parental geothermal fluid upflow under heat pipe conditions with a temperature of 260 °C at the bottom.

work, the following aspects are neglected: (1) compaction and thermal mechanics, such as micro-fracturing by thermal stress and hydro-fracturing by thermal expansion of pore fluid; (2) the effect of chemical concentration changes on fluid thermophysical properties such as density and viscosity, which are considered functions of pressure and temperature only; (3) the enthalpy due to chemical reactions.
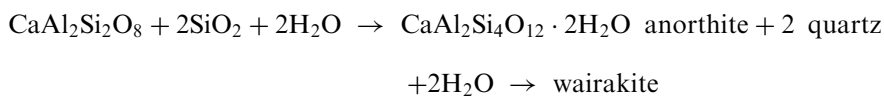
In most modeling cases the host reservoir rocks are assumed to be andesites. Hydrothermal upflow in andesites is very common: 93% of the host reservoir rocks in the studied geothermal fields are andesites, or include andesites, as the principal host rock. Because the current thermodynamic database is incomplete and restricted to end-member phases in solid solution series, several proxy minerals that in aggregate reflect the bulk composition of this host rock were chosen to represent the mineral composition of unaltered andesite. Fortunately, the impact of these necessary substitutions on the described model simulations is minor, because all primary proxy minerals except quartz are unstable with respect to the secondary minerals.

The initial mineral composition of the reservoir is assumed as a pyroxene andesite: 45% anorthite (Ca-feldspar), 26% albite-high (Na-feldspar), 11% sanidine (K-feldspar), 16% diopside, and 2% quartz. Total porosity was assigned a value of 0.1. The kinetic parameters of chemical interaction are given in Table 3. The 'parental geothermal fluid' with a chemical composition corresponding to different geothermal fields (Table 1) was injected into the model geothermal reservoirs (Fig. 3). The following secondary hydrothermal minerals are included in the system (in addition to the source minerals mentioned above): calcite, anhydrite, low-albite, wairakite, laumontite, mordenite, Na, Ca and Mg-smectites, chlorite, illite, amorphous silica, cristobalite, opal, kaolinite and prehnite.

4. Results

4.1. 'No flow' single phase mode

Fig. 7 shows the results for a modeling scenario in which 'no flow' single-phase conditions are specified, and the chemical composition of the parental geothermal fluid of Ogiri geothermal field is used (Table 1). Mineral alteration after 1000 years includes replacement of high albite by low albite, significant precipitation of laumontite and wairakite (0.0032 volume fraction at 240 °C), and dissolution of anorthite and quartz. This can be represented by the reaction:

$$CaAl_2Si_2O_8 + 2SiO_2 + 2H_2O \rightarrow CaAl_2Si_4O_{12} \cdot 2H_2O \text{ anorthite} + 2 \text{ quartz}$$

$$+2H_2O \rightarrow \text{ wairakite}$$

This process is sensitive to rock porosity: if the porosity value is reduced below 0.001, then no significant formation of zeolites would occur because of the limited availability of water in the pore space.
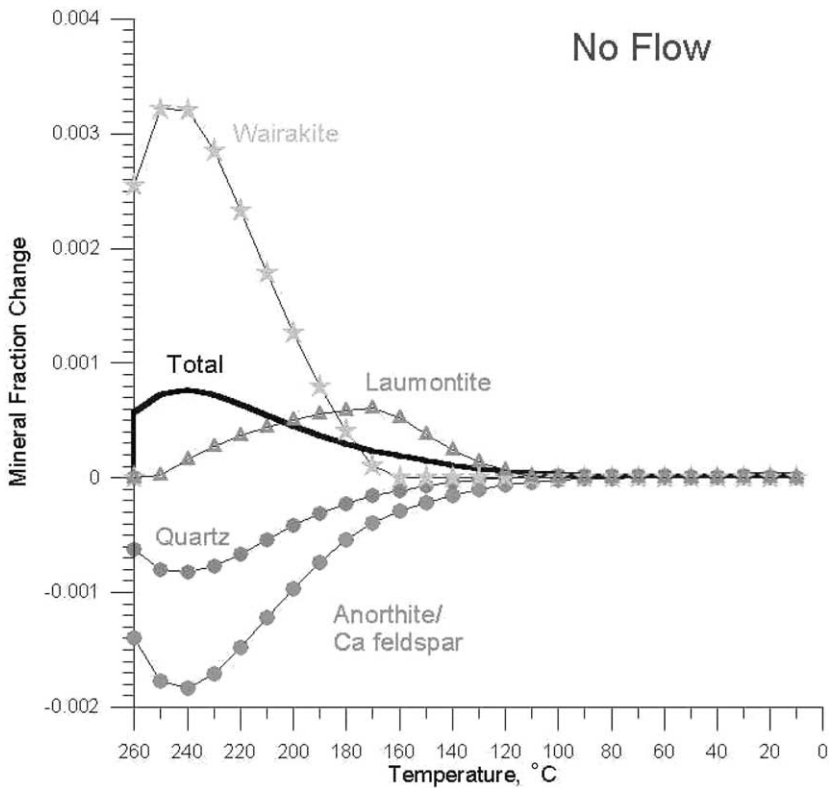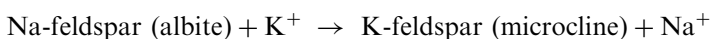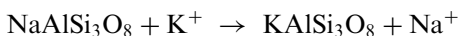
Fig. 7. Change of volume fraction of mineral phases in model reservoir after 1000 years wider 'no flow' single-phase conditions. The chemical composition of the Ogiri parental geothermal fluid was used (Table 1).

4.2. "Massflux mode", single-phase upflow scenario

Fig. 8 shows the mineral phase distribution for a single-phase modeling scenario, where 'mass flux' conditions (2500 kg/s km^2) are specified, and the chemical composition of the Ogiri parental geothermal fluid is used (Table 1). An upflow rate of 35 kg/s is assumed in the model, corresponding to Ginyu fault parameters (Goko, 2000). In this case, upwelling 'parental geothermal fluid' causes significant quartz and K-feldspar precipitation, due to its elevated SiO_2 and $K+$ concentrations. Albite dissolution proceeds as follows:

$$NaAlSi_3O_8 + K^+ \rightarrow KAlSi_3O_8 + Na^+$$

$$\text{Na-feldspar (albite)} + K^+ \rightarrow \text{K-feldspar (microcline)} + Na^+$$
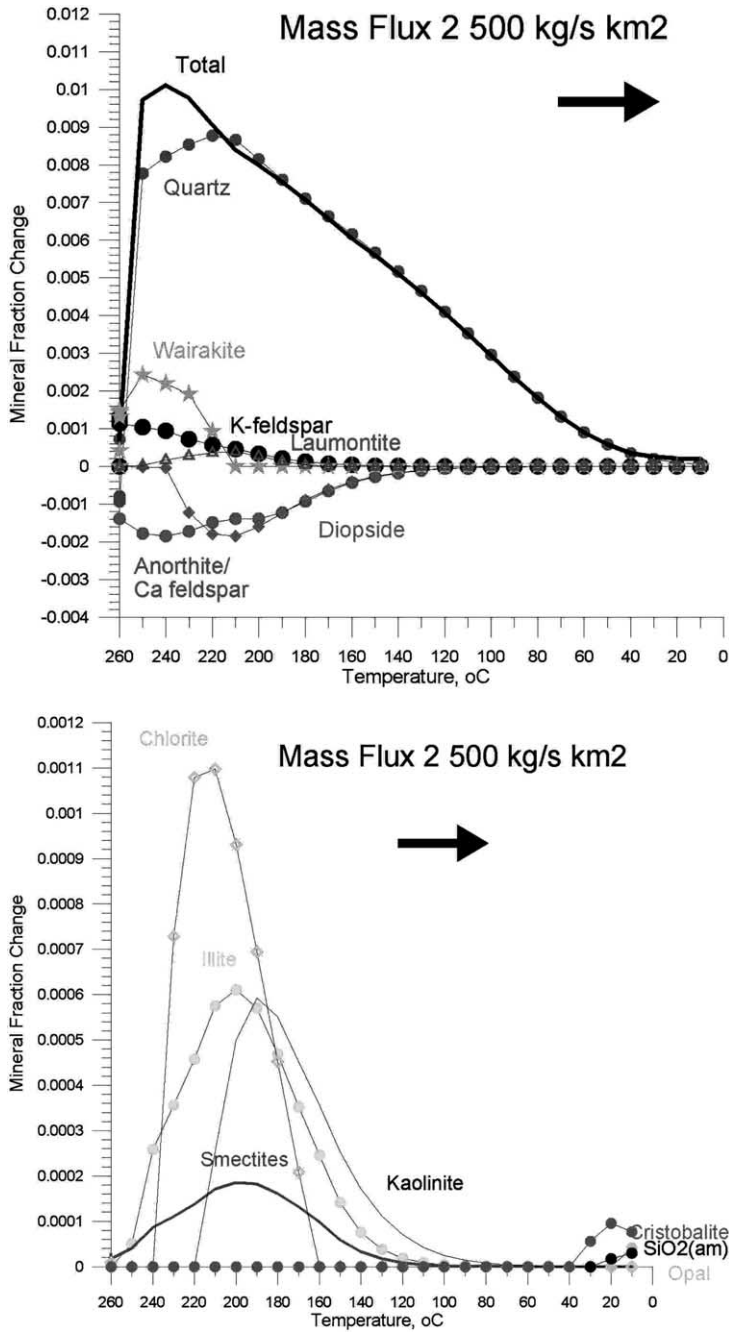
Fig. 8. Change in volume fraction of mineral phases along the ascendiug flow path (mass flux conditions) after 1000 years. Upper figure—principal mineral phases; lower figure—minor mineral phases. The chemical composition of the Ogiri parental geothermal fluid was used (Table 1).

In addition to the replacement of high-albite by low-albite, we also observe precipitation of wairakite (0.0025 volume fraction at 240 °C) and laumontite, and dissolution of the source minerals anorthite and diopside after 1000 years. Significant amounts of chlorite, illite, smectite and kaolinite also precipitate.

4.3. 'Mass flux' mode, two-phase upflow scenario

Figs. 9–12 show changes in abundance of the mineral phases for the two-phase modeling scenario, where mass flux conditions (2500 kg/s km^2) are specified, and the chemical compositions of the Hatchobaru, Sumikawa, Mutnovsky and Uenotai parental geothermal fluids were used, respectively (Table 1). In all cases the principal mineral phases precipitating under two-phase conditions are quartz and microcline, which cause a 0.022 porosity reduction in 1000 years.

The Hatchobaru modeling case shows a large amount of anhydrite, quartz, chlorite and calcite precipitation under liquid-phase conditions in the lower part of the production zone where pressures are above 80 bar, and significant precipitation of quartz and microcline under two-phase conditions below 80 bar, whereas no significant wairakite or laumontite precipitation is observed. Anorthite and diopside dissolve under liquid-phase conditions, while only anorthite dissolves under two-phase conditions (Fig. 9).

The Sumikawa modeling case shows large amounts of anhydrite, microcline and quartz deposition under single-phase conditions (at pressures above 85 bar) (Fig. 10). Some chlorite, epidote and low albite also precipitate under single-phase conditions. Significant quartz, microcline, wairakite and laumontite precipitation under two-phase conditions below 80 bar is observed. Anorthite dissolves, but no diopside dissolution is obtained in the model.

The Mutnovsky modeling case shows quartz and microcline precipitation as principal mineral phases, and chlorite, epidote, low-albite deposition as minor mineral phases under single-phase conditions at pressures above 80 bar (Fig. 11). Quartz, microcline, wairakite, calcite and laumontite precipitate under two-phase conditions below 80 bar. Significant anorthite dissolution and minor diopside dissolution under single-phase conditions were also observed.

The Uenotai modeling results are similar to those for the Mutnovsky geothermal field. Quartz, microcline, calcite, wairakite, laumontite and low-albite are secondary mineral phases under two-phase conditions below 80 bar. Significant anorthite dissolution took place, whereas no diopside dissolution occurred (Fig. 12).

4.4. 'Mass flux' mode, heat pipe scenario

The heat pipe scenario, characterized by almost isothermal conditions along two-phase upflow, results in negligible precipitation. The total porosity reduction due to precipitation is 0.0002 after 1000 year. Chemical interactions involve anorthite and diopside dissolution, and precipitation of small amounts of wairakite (Fig. 13).
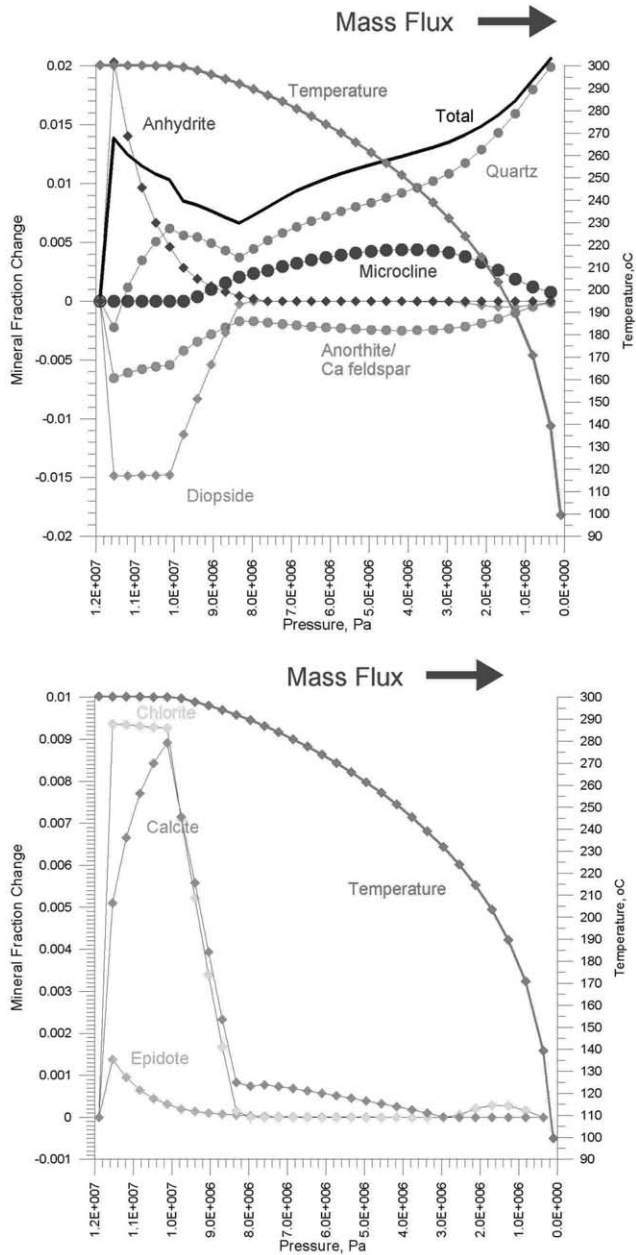
Fig. 9. Change in volume fractions of mineral phases along the ascending flow path (mass flux conditions) after 1000 years. Upper figure—principal mineral phases; lower figure—minor mineral phases. The chemical composition of the Hatchobaru parental geothermal fluid was used (Table 1).
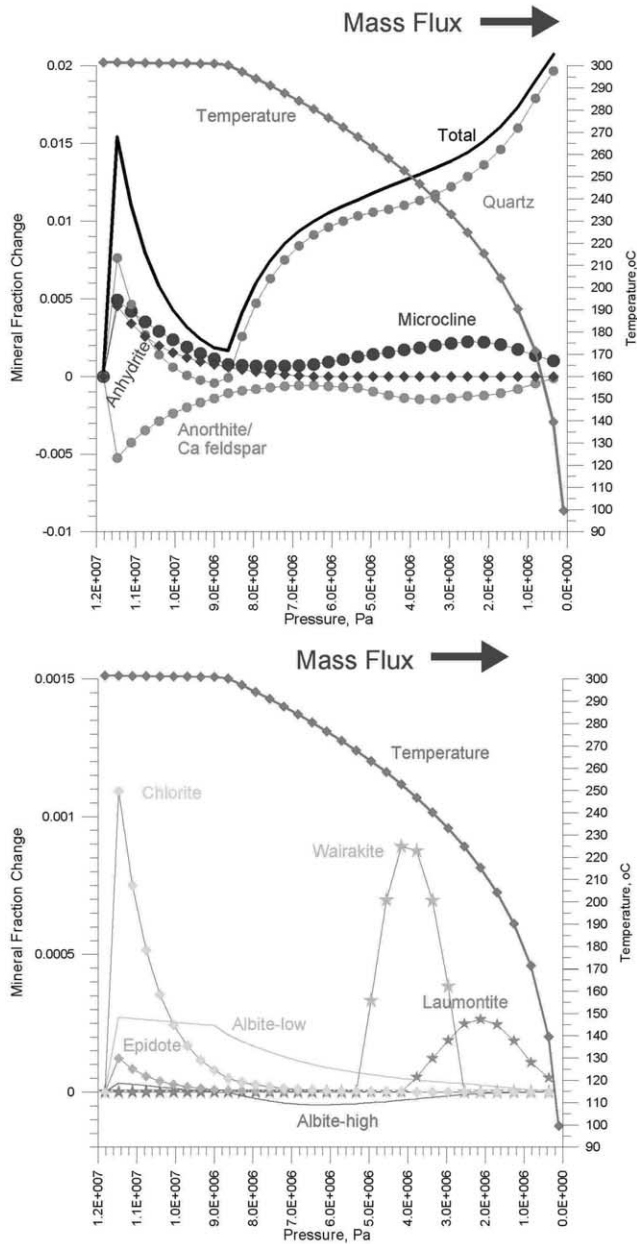
Fig. 10. Change in volume fractions of mineral phases along the ascending flow path (mass flux conditions) after 1000 years. Upper figure—principal mineral phases; lower figure—minor mineral phases. The chemical composition of the Sumikawa parental geothermal fluid was used (Table 1).
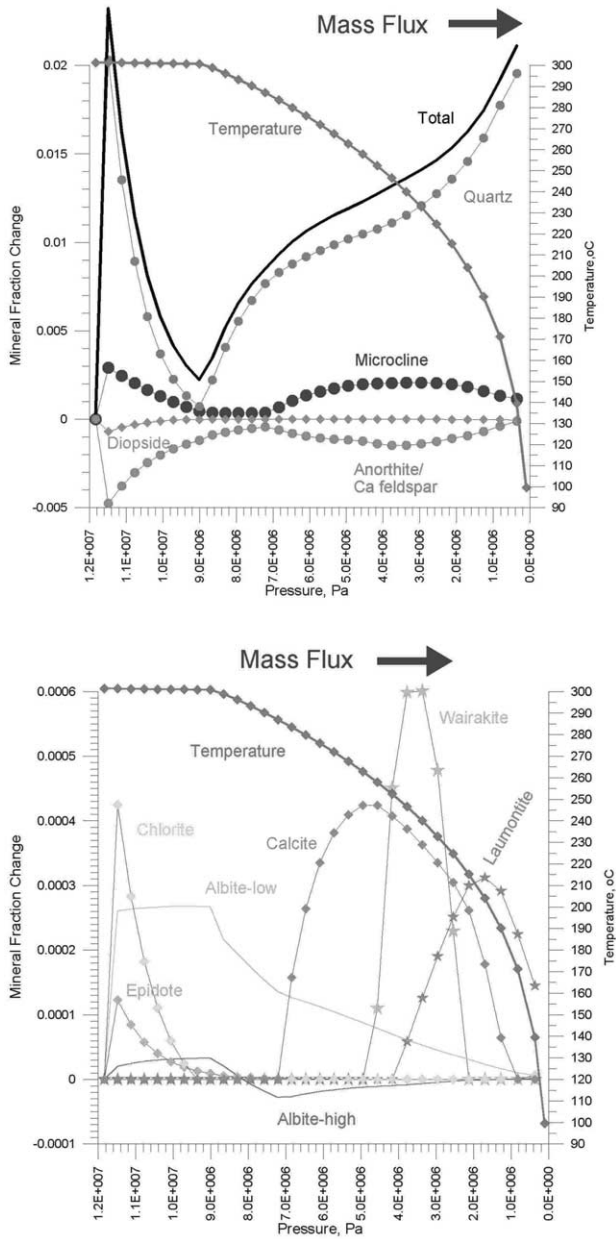
Fig. 11. Change in volume fractions of mineral phases along the ascending flow path (mass flux conditions) after 1000 years. Upper figure—principal mineral phases; lower figure—minor mineral phases. The chemical composition of the Mutnovsky parental geothermal fluid was used (Table 1).
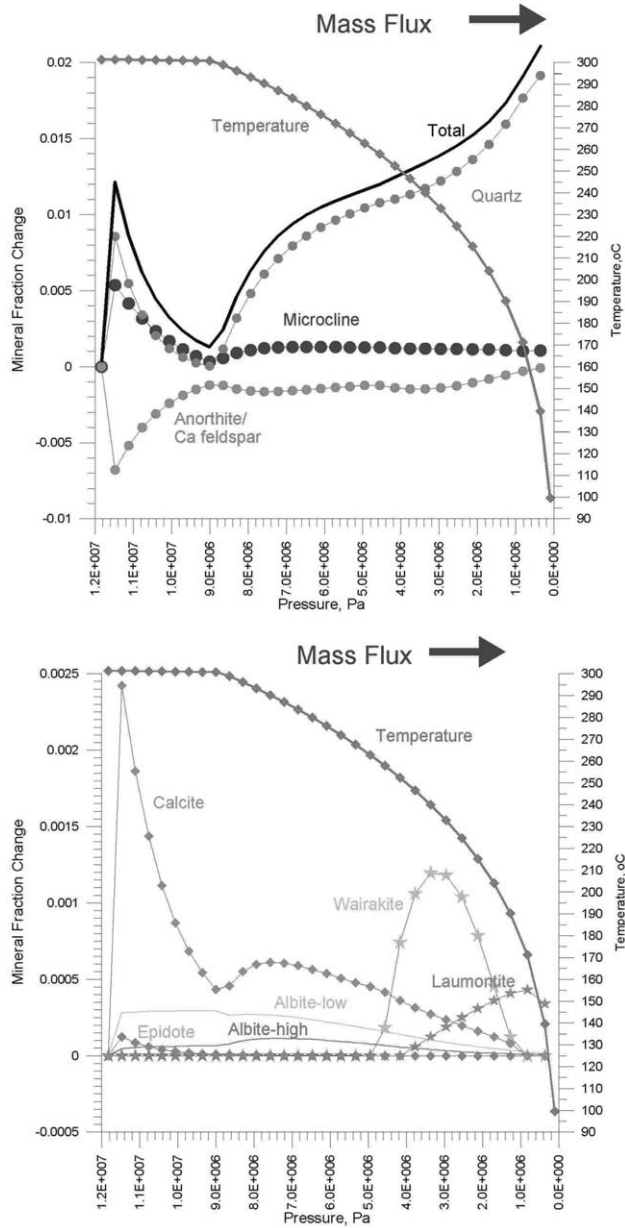
Fig. 12. Change in volume fractions of mineral phases along the ascending flow path (mass flux conditions) after 1000 years. Upper figure—principal mineral phases; lower figure—minor mineral phases. The chemical composition of the Uenotai parental geothermal fluid was used (Table 1).

5. Discussion of modeling results

5.1. Comparison with field data

5.1.1. Single-phase scenario (Table 4)

Wairakite, quartz, K-feldspar and chlorite precipitates are obtained in the model as principal secondary minerals in the production zone, and the illite-smectite maximum at 200 °C matches observations in the Ogiri geothermal field. A core sample from the upper part of the Ginyu fault of Ogiri geothermal field (well KE1-2) shows a 1740 mm vein filled with wairakite and quartz at 222 °C (Goko, 2000). Secondary K-feldspar was also detected in the Ginyu fault (well NT-Al) (Goko, 2000). Drilling observations show that chlorite-smectite indicate proximity to the Ginyu fault, and whether or not a well has been drilled completely through the fault zone (Goko, 2000).

5.1.2. Two-phase scenario

Quartz, K-feldspar (microcline), wairakite and calcite commonly appear as the principal secondary minerals in two-phase production zones. This is matched by observations at the Hatchobaru, Sumikawa, Mutnovsky and Uenotai geothermal
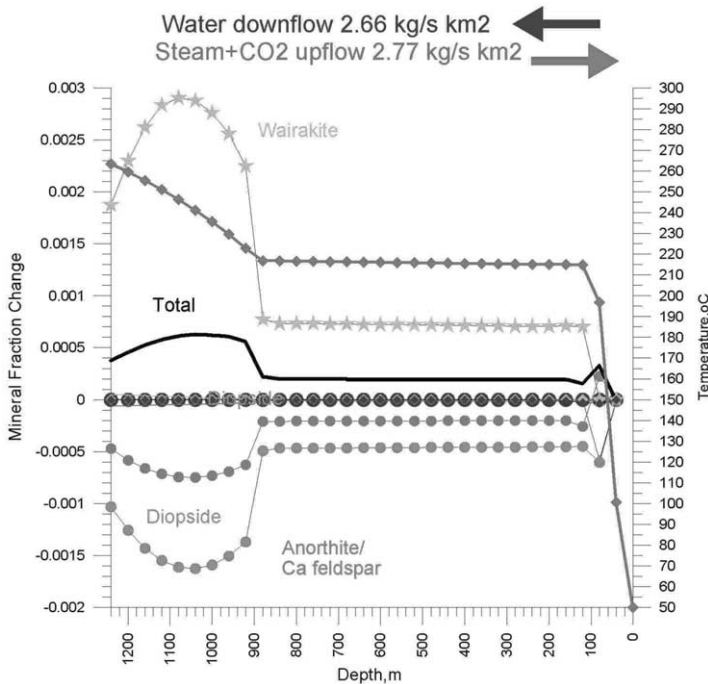

Fig. 13. Change in volume fractions of mineral phases along the ascending flow path (mass flux conditions) after 1000 years. The chemical composition of the Matsukawa parental geothermal fluid was used (Table 1).

fields (Table 4). It is also observed in the model that low pH, high gas (CO_2) content and increase of fluid species mineralization suppress wairakite precipitation and favor diopside dissolution (see the model results for Hatchobaru).

5.1.3. Heat pipe scenario

The absence of any significant quartz, feldspar or zeolite precipitation compares well with observations at the Matsukawa geothermal field.

5.2. Model calibration

Calibration of the models to field observation was accomplished through adjustment of the effective surface areas of the minerals, rather than by adjustment of the dissolution or precipitation kinetics. Inappropriate minerals were also eliminated, i.e. those that were not favored for kinetic reasons, or whose appearance was inconsistent with field conditions, and whose thermodynamic data were suspect. To ensure that quartz precipitation occurred in quantities consistent with field observation, the surface areas of reactant feldspars and secondary smectites were reduced

Table 3
Kinetic parameters for chemical interaction (k—chemical dissolution/precipitation kinetic rate constant at 25 °C, mol/s m^2, S—surface area, m^2/m^3, and E_a-activation energy, kJ/kmol)

Minerals	Formulae	k mol/s m^2	S m^2/m^3	E_a kJ/mol
		Minerals at equilibrium		
Calcite	$CaCO_3$			
Anhydrite	$CaSO_4$			
Quartz	SiO_2	4.3e-14	1.0e+3	75.0
Microcline (K-feldspar)	K $AlSi_3O_8$	1.0e-12	1.1e-3	67.83
Albite—high (Na-feldspar)	Na $AlSi_3O_8$	1.0e-12	2.6e-4	67.83
Albite—low (Na-feldspar)	Na $A1Si_3O_8$	1.0e-12	1.0e-4	67.83
Anorthite (Ca-feldspar)	Ca $Al_2Si_2O_8$	1.0e-12	4.5e-2	67.83
Diopside	$CaMgSi_2O_6$	1.0e-12	1.8e-1	67.83
Cristobalite-a	SiO_2	3.4491e-13	1.0e+3	68.9
Opal	SiO_2	3.4491e-13	1.0e+3	68.9
Amorphous silica	SiO_2	7.3234e-13	1.0e+3	62.9
Wairakite	$Ca[Al_2Si_4O_{12}]\,2H_2O$	2.5e-13	1.0e+2	58.0
Laumontite	$Ca[A1_2Si_4O_{12}]\,4H_2O$	2.5e-13	1.0e-2	58.0
Mordenite	$(Na_2,K_2,Ca)\,[Al_2Si_{10}O_{24}]\,7H_2O$	2.5e-13	1.0e-1	58.0
Illite	K $Al_4\,[Si_7AlO_{20}](OH)_4$	1.0e-14	1.0e-1	58.62
Ca-smectite	$Ca_{0.3}Al_{3.5}Mg_{0.5}\,(Si_8O_{20})(OH)_4$	1.0e-14	1.0e-3	58.62
Mg-smectite	$MgAl_{3.5}(Si_8O_{20})(OH)_4$	1.0e-14	1.0e-3	58.62
Na-smectite	$Na_{0.6}A1_{3.5}Mg_{0.5}\,(Si_8O_{20})(OH)_4$	1.0e-14	1.0e-3	58.62
Chlorite	$Mg_{10}Al_2\,[Si_6Al_2O_{20}](OH)_{16}$	1.0e-14	1.0e+1	58.62
Kaolinite	$Al_4[Si_4O_{10}](OH)_8$	1.0e-13	1.0e-1	62.76

Notes: k and E_a values: quartz, feldspars, chlorite, illite, smectites, and kaolinite from Xu and Pruess (2001a); cristobalite, opal, amorphous silica, zeolites (wairakite, laumontite, mordenite) from E. Sonnenthal (personal communication, 2002); diopside kinetic parameters set to those of the feldspars. S (surface area) values are calibrated in the model.

Table 4
Principal secondary minerals in the production reservoirs of the geothermal fields: confirmed by field observations and modelling

Geothermal field	Base temperature °C and phase conditions	Production reservoir host rocks	Principal secondary hydrothermal minerals occurence													
			Quartz	K-feldspar	Na-feldspar	Wairakite	Laumontite	Calcite	Anhydrite	Chlorite	Illite	Smectites	Epidote	Prehnite	Sericite	Kaolinite
Matsukawa	250 steam	Dacite and rhyolite welded tuffs											⊕			
Sumikawa	300 2-phase	Andesites and granitcs	●	●		●	●		●	●			●			
Uenotai	300 2-phase liquid	Andesites and granite	●			●		●		●			●			
Hatchobaru	300 liquid	Pyroxene andesites	●		●	●	⊕	●	●	●			●			
Ogiri	232 liquid	Pyroxene andesites	●	●		●				●			⊕			
Mutnovsky	300 liquid, 2-phase	Diorites, sandstones, rhyolite, andesite tuffs and lavas	●			●	●	●		●	⊕		●	⊕		

Black dots: confirmed by field observations; circles with cross: not confirmed by modelling.

considerably (Table 3). We can only speculate on the underlying basis for this required adjustment at this time. Both specific surface areas and mineral dissolution or precipitation kinetics are subject to large uncertainties, which may be related to the petrofabric of the host rocks, to defect structures in the minerals, or to inhibitory processes due to sorption of dissolved molecular or ionic species. The initial simulations also resulted in an overwhelming preponderance of secondary prehnite formation. No satisfactory explanation could be found for this phenomenon, so that prehnite was eliminated from the model. The thermodynamic data currently available for prehnite and used in the model are in reasonable agreement with recent data by Holland and Powell (1998). It is possible that prehnite formation is kinetically hindered, but resolution of this matter must await further study.

The calibration procedure described above is somewhat arbitrary, and reflects the current uncertainties in adequately defining mineral dissolution kinetics and in specifying mineral reactive surface areas in the model. Recent studies by Lasaga and co-workers (Lasaga and Luttge, 2001) reveal that mineral dissolution kinetics are highly non-linear, especially in the presence of crystal defect structures. Furthermore, the current algorithm describing heterogeneous reaction kinetics does not adequately reflect geochemical processes consistent with the so-called Ostwald Rule of Stages. For example, polymorphs with identical mineral stoichiometries, e.g., the silica polymorphs, precipitate simultaneously in our model; a process that is effectively prohibited by the rule. Similar arguments might likewise be advanced with respect to the relative appearance and stability of wairakite and laumontite in geothermal systems (see below). These issues and others recognized during the course of this study highlight the need for a more sophisticated approach to reactive transport modeling than has hitherto been considered. Nevertheless, the results presented here are encouraging, and form the basis for identifying those issues that require further attention in future refinements to the THC modeling of geothermal processes.

5.3. Porosity reduction

Significant porosity reduction results from convective transport (Fig. 14). Under no-flow conditions, the porosity reduction was 0.0002 (in part through zeolite precipitation) after 100 years; under flowing conditions and a mass flux of 25 kg/s km^2 the porosity reduction (by quartz, zeolites, and additionally by K-feldspar) was 0.0010 after the same time. Significantly greater porosity reductions occur for larger mass fluxes.

The following discussion is a brief interpretation of the key chemical interactions that cause porosity reduction in the fracture system in mass flux conditions.

5.3.1. Quartz and K-feldspar

The concentration of SiO_2 and the Na^+/K^+ ratio in solution under upflow conditions is largely determined by buffering reactions with coexisting reactant and product minerals, as alluded to earlier (Kiryukhin et al., 2002). Fig. 15 illustrates the buffering phenomena as a function of temperature and log $[SiO_2(aq)]$ and log Na^+/K^+, respectively. Quartz solubility control is effective between 260 °C and 120 °C.
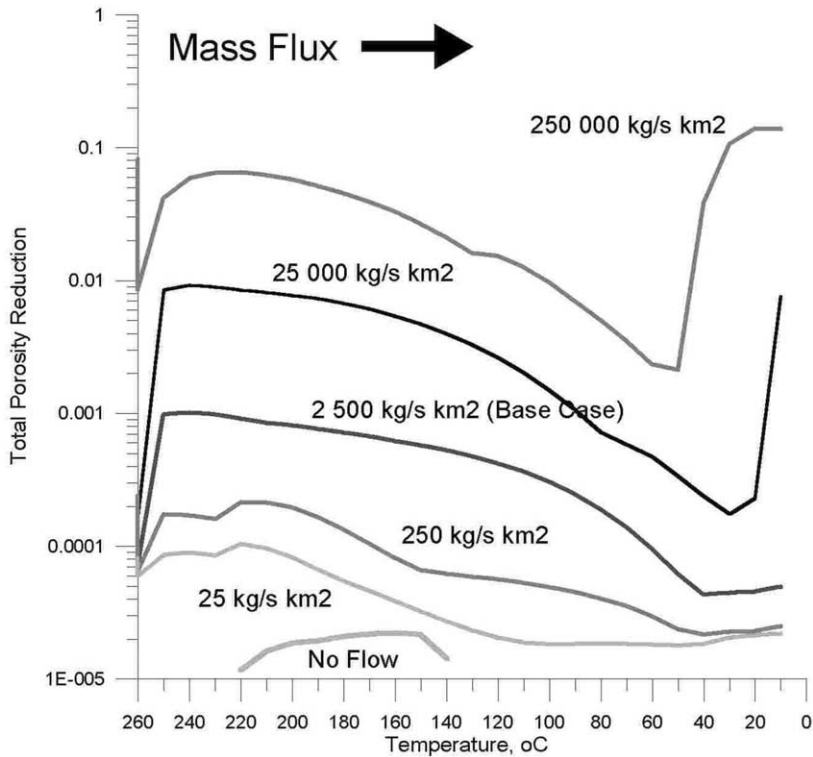
Fig. 14. Porosity reduction along an ascending flow path at different mass fluxes (0–250,000 kg/s km^2) after 100 years, single-phase scenario.

Below the latter temperature, the solution becomes supersaturated with respect to quartz. With respect to log $Na+/K+$, the hydrothermal fluid composition lies within the low-albite stability field between 260 °C and 200 °C, before the fluid becomes supersaturated with respect to K-feldspar. Below 200 °C, K-feldspar precipitation is kinetically controlled.

5.3.2. Zeolites

Mass flux conditions do not significantly influence the temperature dependence of the production of zeolites (wairakite at 220–260 °C, and laumontite at 180–240 °C) with respect to 'no-flow' conditions (wairakite 180–260 °C, and laumontite 140–240 °C). All the chemical components necessary for zeolites are available in the water-saturated andesites (if the porosity value is over 0.001), as discussed above. Some extension of the laumontite temperature range is caused by additional water inflow into the system (laumontite formation requires an additional two moles of H_2O, compared to wairakite).
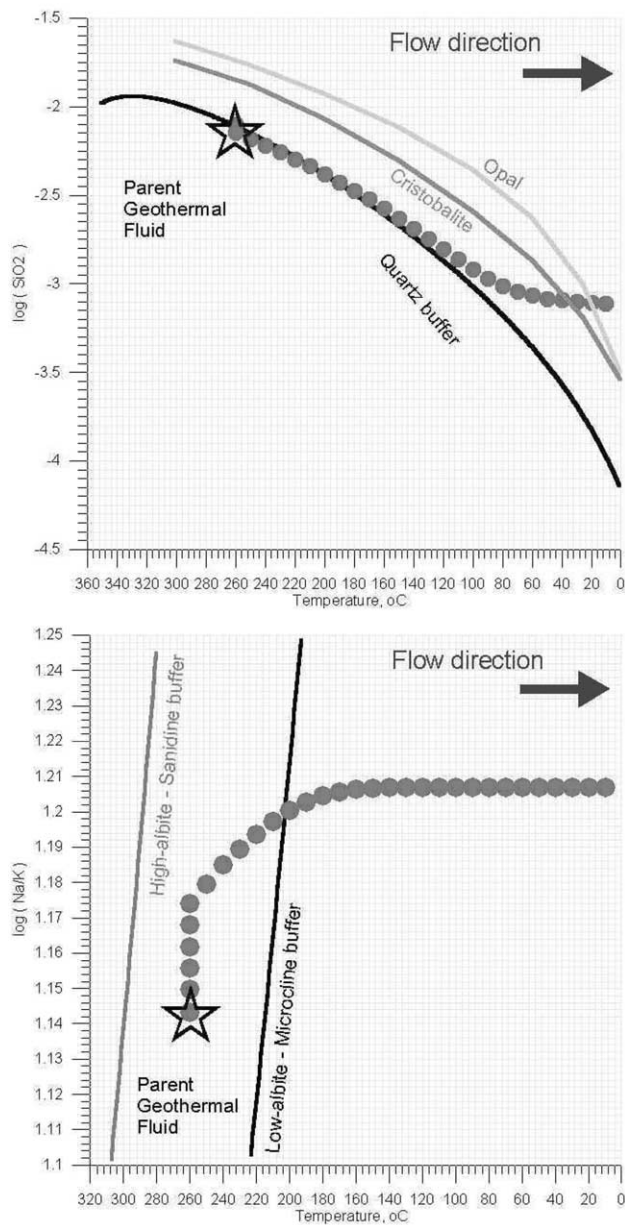
Fig. 15. Temperature equilibrium fluid buffers for single-phase scenario. Upper figure—distribution of $\log(SiO_2)$ along the ascending flow path after 1000 years. SiO_2 fluid temperature buffer $[\log(SiO_2) = f(T)]$ is based on quartz equilibrium under saturated conditions. Kinetic effects may displace the concentration from equilibrium at low temperatures (under 120 °C) as shown above. Lower figure—distribution of $\log(Na/K)$ along the ascending flow path after 1000 years. Na/K fluid temperature buffer $[\log(Na/K) = f(T)]$ is based on the albite/microcline equilibrium under saturated conditions. Kinetic effects may displace the reaction from equilibrium at temperatures under 200 °C, as shown above.

5.4. Wairakite-laumontite thermodynamic problem

The lowest wairakite-to-laumontite conversion temperatures obtained in the model are 220/180 °C. This is a reasonable match to the Takigami geothermal field (200/150 °C) (Furuya et al., 2000) and Pauzhetsky geothermal field (max temperature 220 °C) (Pauzhetka, 1965), where mostly laumontite was reported. In contrast, only wairakite was reported in the Ginyu fault production zone at Ogiri (Goko, 2000), although a similar range of temperatures, fluid chemistry and host rock composition is present. One possible explanation is the small difference in wairakite/laumontite thermodynamic properties in the 200–250 °C range of temperatures, which make their occurrence very sensitive to small changes in source rock and fluid chemistry (Fig. 16).

6. Conclusions

The data available on secondary mineral distributions, host rock properties and chemical composition of parental geothermal fluids of 14 geothermal fields in Japan
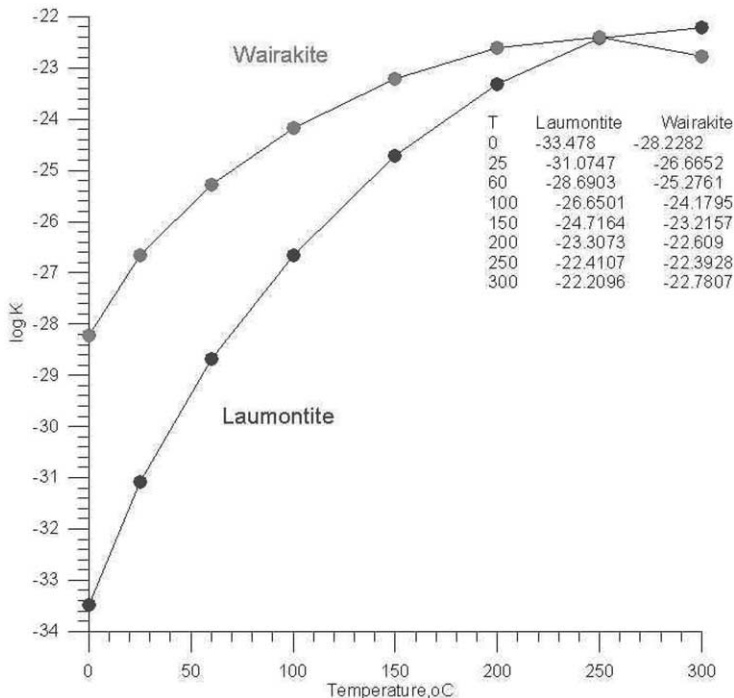

Fig. 16. Wairakite and laumontite equilibrium constants (log K) vs. temperature. Note that the difference in log K between wairakite and laumontite at 230 °C (503 K) is only 0.4, equivalent to 0.4 RT 2.303 = 3.8 kJ/mol, which is within the uncertainty of the thermodynamic data used in the simulation.

and Kamchatka (Russia) have been used for the calibration of a thermal–hydro-dynamic–chemical (THC) model.

THC modeling of the liquid upflow at 260 °C in andesites, represented by the Ogiri, Japan, geothermal field, was selected as representative of the single-phase upflow scenario. Wairakite, quartz, K-feldspar and chlorite formed in the model as the principal secondary minerals in the production zone, and illite-smectite formed below 230 °C. These results match observations in the Ogiri geothermal field.

THC modeling of the two-phase upflow at 300 °C in andesites, represented by the Hatchobaru, Sumikawa, Uenotai (Japan) and Mutnovsky (Kamchatka, Russia) geothermal fields, was selected as representative of the two-phase upflow scenario. Quartz, K-feldspar (microcline), wairakite and calcite precipitate in the model as principal secondary minerals in the production zone. These results match observations in the Hatchobaru, Sumikawa, Uenotai (Japan) and Mutnovsky (Kamchatka, Russia) geothermal fields.

THC modeling of heat pipe conditions, represented by the Matsukawa (Japan) geothermal field, was selected as representative of heat pipe conditions. The modeling study shows no significant secondary deposition of minerals (quartz, K-feldspar, zeolites) in the two-phase isothermal conditions of the production zone. These results match observations in the Matsukawa geothermal field.

THC modeling shows a significant influence of the thermodynamic and kinetic parameters of chemical interaction, and of mass flux on mineral phase formation along the ascending flow path. No parental geothermal fluid inflow is apparently needed for zeolite precipitation, which occurs above 140 °C in saturated andesite, provided that the porosity is greater than 0.001. Quartz and K-feldspar precipitation may result in significant porosity reduction over a 100-year time scale under mass flux conditions, and complete fracture sealing will occur given sufficient time under either single-phase or two-phase upflow scenarios, while the heat pipe scenario shows no significant porosity reduction due to lack of secondary mineral phase deposition.

Further enhancements of the THC model of active hydrothermal systems are required and should include refinements to some assumptions and parameters, including the thermodynamic and kinetic databases, and the development of more sophisticated algorithms describing heterogeneous reaction kinetics. The application of the model to other geothermal fields is also desirable.

Appendix. Mathematical equations used in the model

Table A1.
Governing equations for fluid and heat flow, and chemical transport (meanings of symbols are given in Table A2)

General governing equations:	$\dfrac{\partial M_\kappa}{\partial t} = -\nabla F_\kappa + q_\kappa$	
Water: $M_w = \phi\big(S_1\rho_1 X_{w1} + S_g\rho_g X_{wg}\big)$	$F_w = X_{w1}\rho_1\mathbf{u}_1 + X_{wg}\rho_g\mathbf{u}_g$	$q_w = q_{w1} + q_{wg}$
CO_2: $M_c = \phi\big(S_1\rho_1 X_{c1} + S_g\rho_g X_{cg}\big)$	$F_c = X_{c1}\rho_1\mathbf{u}_1 + X_{cg}\rho_g\mathbf{u}_g$	
$q_c = q_{c1} + q_{cg} + q_{cr}$		
Heat: $M_h = \phi\big(S_1\rho_1 U_1 + S_g\rho_g U_g\big) + (1-\phi)\rho_s U_s$	$F_h = \sum_{\beta-1,g} h_\beta\rho_\beta\mathbf{u}_\beta - \lambda\nabla T$	q_h
where $u_\beta = -k\dfrac{k_{r\beta}}{\mu_\beta}\big(\nabla P_\beta - \rho_\beta\mathbf{g}\big)\beta = 1,g$	(Darcy's Law)	
Chemical components in the liquid phase ($j = 1,2,\dots,N_1$):	$F_j = \mathbf{u}_1 C_{j1} - (\tau\phi S_1 D_1)\nabla C_{j1}$	$q_j = q_{j1} + q_{js} + q_{jg}$
$M_j = \phi S_1 C_{j1}$	$\tau_\beta = \phi^{1/3} S_\beta^{7/3}$	

Table A2.
Symbols used in Table A1

C	component concentration, mol L^{-1}	ρ	density, kg m^{-3}
D	diffusion coefficient, $m^2\ s^{-1}$	μ	viscosity, kg $m^{-1}\ s^{-1}$
F	mass flux, kg $m^2\ s^{-1}$ [a]	λ	heat conductivity, W $m^{-1}\ K^{-1}$
K	permeability, m^2	τ	medium tortuosity
k_r	relative permeability		
G	gravitational acceleration, m s^{-2}	Subscripts	
M	mass accumulation, kg m^{-3}	c	CO_2
N	number of chemical components	g	gas phase
P	pressure, Pa	h	heat
q	source/sink	j	aqueous chemical component

S	saturation	l	liquid phase
T	temperature, °C	r	reaction
U	internal energy, J kg^{-1}	s	solid phase
u	Darcy velocity, m s^{-1}	w	water
X	mass fraction	κ	governing equation index
Φ	porosity	β	phase index

[a] For chemical transport and reaction calculations, molar units are used instead of kg.

References

Ariki, K., Kato, H., Ueda, A., Bamba, M., 2000. Characteristics and management of the Sumikawa geothermal reservoir, northeastern Japan. Geothermics 29, 171–189.

Fujino, T., Yamasaki, T., 1984. Geologic and geothermal structure of the Hatchobaru field, central Kyushu, Japan. Geothermal Resources Council Transactions 8, 425–430.

Furuya, S., Aokia, M., Gotoha, H., Takenaka, T., 2000. Takigami geothermal system, northeastern Kyushu, Japan. Geothermics 29, 191–211.

Goko, K., 2000. Structure and hydrology of the Ogiri field, West Kirishima geothermal area, Kyushu, Japan. Geothermics 29, 127–149.

Hanano, M., Matsuo, G., 1990. Initial state of the Matsukawa geothermal reservoir: reconstruction of a reservoir pressure profile and its implications. Geothermics 19, 541–560.

Hayashi, M., Mimura, T., Yamasaki, T., 1978. Geological setting of reinjection wells in the Otake and Hatchobaru geothermal field, Japan. Geothermal Resources Council Transactions 2, 337–340.

Holland, T., Powell, R., 1998. An internally consistent thermodynamic dataset for phases of petrological interest. Journal of Metamorphic Geology 16, 309.

Higo, M., 1985. Geothermal country update of Japan. Proc. International Symposium on Geothermal Energy, Hawaii, pp. 119–134.

Kiryukhin, A.V., 1993. High temperature fluid flows in the Mutnovsky hydrothermal system, Kamchatka. Geothermics 23, 49–64.

Kiryukhin, A.V., 1996. Modeling studies: the Dachny geothermal reservoir, Kamchatka, Russia. Geothermics 25, 63–90.

Kiryukhin, A., Xu, T., Pruess, K., Slovtsov, I., 2002. Modeling of thermo–hydrodynamic-chemical processes: some applications to active hydrothermal systems. 27th Stanford Workshop on Geothermal Reservoir Engineering, pp. 140–147.

Lasaga, A., Luttge, A., 2001. Variation of crystal dissolution rate based on a dissolution stepwave model. Science 291, 2400–2404.

Matsuyama, K., Narita, N., Tomita, K., Majima, T., 2000. Geothermal resources of Hachijojima. Geothermics 29, 213–232.

Mizugaki, K., 2000. Geologic structure and volcanic history of the Yanaizu-Nishiyama (Okuaizu) geothermal field, Northeast Japan. Geothermics 29, 233–256.

Muraoka, H., Uchida, T., Sasada, M., Yagi, M., Akaku, K., Sasaki, M., Yasukawa, K., Miyazaki, S., Doi, N., Saito, S., Sato, K., Tanaka, S., 1998. Deep geothermal resources survey program: igneous, metamorphic and hydrothermal processes in a well encountering 500 °C at 3729 m depth, Kakkonda, Japan. Geothermics 27, 507–534.

Naka, T., Okada, H., 1992. Exploration and development of Uenotai geothermal field, Akita prefecture, northeastern Japan. Resource Geology 42, 223–240 (in Japanese with English abstract).

Narasimhan, T.N., Witherspoon, P.A., 1976. An integrated finite difference method for analyzing fluid flow in porous media. Water Resource Res. 12, 57—64.

Nitta, T., Tsukagoshi, S., Adachi, M., Seo, K., 1995. Exploration and development in the Okuaizu geothermal field, Japan. Resource Geol. 45, 201–212 (in Japanese with English abstract).

Okada, H., Yasuda, Y., Yagi, M., Kai, K., 2000. Geology and fluid chemistry of the Fushime geothermal field, Kyushu, Japan. Geothermics 29, 279–311.

Pauzhetka Thermal Waters in Kamchatka, 1965. Nauka Publ, Moscow.

Pruess, K., 1991. TOUGH2: A General Numerical Simulator for Multiphase Fluid and Heat Flow. Lawrence Berkeley Laboratory Report LBL-29400, Berkeley, CA.

Reed, M., Spycher, N., 1984. Calculation of pH and mineral equilibria in hydrothermal waters with application to geothermometry and studies of boiling and dilution. Geochim. Cosmochim. Acta 48, 1479–1492.

Reed, M.H., 1982. Calculation of multicomponent chemical equilibria and reaction processes in systems involving minerals, gases and aqueous phase. Geochim. Cosmochim. Acta 46, 513–528.

Steefel, C.I., Lasaga, A.C., 1994. A coupled model for transport of multiple chemical species and kinetic precipitation/dissolution reactions with applications to reactive flow in single phase hydrothermal system. Am. J. Sci. 294, 529–592.

Takeno, N., 2000. Thermal and geochemical structure of the Uenotai geothermal system, Japan. Geothermics 29, 257–277.

Ueda, A., Kubota, Y., Katoh, H., Hatakeyama, K., Matsubaya, O., 1991. Geochemical characteristics of the Sumikawa geothermal system, northeast Japan. Geochemical Journal 25, 223–244.

White, S.P., 1995. Multiphase non-isothermal transport of systems of reacting chemicals. Water Resource Res. 31, 1761–1772.

Wolery, T.J., 1992. EQ3/6: Software Package for Geochemical Modeling of Aqueous Systems: Package Overview and Installation Guide (Version 7.0). Lawrence Livermore National Laboratory Report UCRL-MA-1 10662 PT I, Livermore, CA, 1992.

Xu, T., Pruess, K. 1998. Coupled Modeling of Non-isothermal Multiphase Flow, Solute Transport and Reactive Chemistry in Porous and Fractured Media: 1. Model Development and Validation. Lawrence Berkeley National Laboratory Report LBNL-42050, Berkeley, CA.

Xu, T., Pruess, K.On Fluid Flow and Mineral Alteration in Fractured Caprock of Magmatic Hydrothermal Systems. Journal of Geophysical Research 106 (B2), 2121–2138.

Xu, T., Pruess, K., 2001b. Modeling multiphase non-isothermal fluid flow and reactive geochemical transport in variability saturated fractured rocks: methodology. Am. J. Sci. 301, 16–33.

Yamada, M., Iguchi, K., Nakanishi, S., Todaka, N., 2000. Reservoir characteristics and development plan of the Oguni geothermal field, Kyushu, Japan. Geothermics 29, 151–169.

Yoshida, Y., 1984. Origin of gases and chemical equilibrium among them in steams from Mataukawa geothermal area, northeast Japan. Geochemical Journal 18, 195–202.